3D shape shearography technique for surface strain measurement of free-form objects

Anisimov, Andrei G.; Serikova, Mariya G.; Groves, Roger M.

DOI
10.1364/AO.58.000498

Publication date
2019

Document Version
Final published version

Published in
Applied Optics

applied optics

3D shape shearography technique for surface strain measurement of free-form objects

Andrei G. Anisimov,[1,*] Mariya G. Serikova,[2] and Roger M. Groves[1]

[1]Aerospace Non-Destructive Testing Laboratory, Delft University of Technology, Kluyverweg 1, 2629 HS, Delft, The Netherlands
[2]Department of Optical-Electronic Devices and Systems, ITMO University, Kronverksky 49, Saint Petersburg 197101, Russia
*Corresponding author: a.g.anisimov@tudelft.nl

Received 16 October 2018; revised 3 December 2018; accepted 4 December 2018; posted 5 December 2018 (Doc. ID 348519); published 11 January 2019

Shearography is a non-destructive testing technique that provides full-field surface strain characterization. Previous inspection of flat objects or simple geometric shapes has been reported. However, real-life objects especially in aerospace, transport, or cultural heritage are not flat, but their inspection with shearography is of interest for both hidden defect detection and material characterization. Accurate strain measurement of a highly curved or free-form surface needs to be performed by combining in-line object shape measuring and processing of the shearography data in 3D. Previous research has not provided a general solution for that. This paper presents a new approach of 3D shape shearography which is based on the integration of a structured light projector for in-line shape measuring with 3D shearography. For the experimental part, a 3D shape shearography system prototype was developed and its performance was evaluated with a cylinder specimen loaded by internal pressure and compared with strain gauges.

https://doi.org/10.1364/AO.58.000498

1. INTRODUCTION

Shearography (speckle pattern shearing interferometry) is a coherent-optical inspection technique [1,2] often used for non-destructive testing and surface strain measurement [3]. Being an imaging technique, shearography provides full-field measurements in a non-contact way. Shearography has a direct sensitivity to the surface displacement gradient providing a quantitative measurement of surface strain components [2,3]. Six surface displacement gradient components, including in- and out-of-plane components can be measured with well-known multicomponent shearography instruments with three or more viewing or illumination directions [4,5].

The shearography technique is capable of measuring the surface strain components if the information about an object, its shape, and location is known and telecentric imaging is used [2,3]. In the case of a flat small object, the data processing can be simplified with certain assumptions, such as constant shear distances [2] together with constant sensitivity vectors within the field of view [6]. Therefore, mostly flat objects at a known distance were inspected before [2,3]. However, many objects of interest for the inspection are curved, e.g., leading edges in aerospace, sculptures in heritage. Their inspection with shearography is also of an interest for both hidden defect detection and characterization of the material behavior under various loading scenarios. Therefore, the location, orientation, and shape have to be measured for curved objects, preferably in-line [4,7]. Three approaches to apply shearography to curved surfaces discussed below were found in the literature; however, none of them provides a general solution for strain measuring of a free-form object with an unknown orientation.

The first approach is to generate interferometric carrier fringes and to project them on the object to perform profilometry [8–11]. For this, a displacement of the laser source is used resulting in a posterior revealing of carrier fringes and determining the object shape from their analysis [10]. This approach results in a compact, single optical path shearography system, but in practice, it has limited measuring performance because of the fringe distortion and difficulties in data processing. In [11] shape measurement was combined with out-of-plane displacement gradient measurement with shearography. The interferometric combination of shearography with the electronic speckle pattern interferometry (ESPI) technique was also reported [12] to get in-line shape information at the laser wavelength scale; however, a measuring range in the millimeter and centimeter scales was not possible.

Another approach uses virtual reality techniques and strain data mapping onto 2D or 3D surfaces (e.g., a canvas painting) [13–16], CAD models, or real surface profiles measured with various topography or shape measuring techniques [12,17,18]. In some cases, UV-mapping [15,19] is used for fusion of the topography and shearography data. Several developments used structured light projectors to measure the shape [14–16] or to

project the shearography phase maps on the object for interactive visualization [20,21]. Although the 3D shape measurement approach was mentioned in a short report [22], the authors did not report on the use of the surface data for correction of the shear distances or the sensitivity vectors. In summary, the 3D data was mostly used as a basis for visualization and data fusion, rather than for precise strain measurement.

Shearography with precise mapping of the surface strain components onto curved objects has also been reported [10,23,24]. This mapping is based on the assumptions that the location, orientation, and shape of the object are known in advance, so all these parameters can be predefined parametrically. Therefore, this technique is not applicable to free-form surfaces with arbitrary location.

The need for the precise surface strain mapping onto real curved objects is supported by numerous applications of shearography in aerospace [2,3,18], e.g., airplane and automotive tires inspection [2,25], inspection of inner cylindrical surfaces using endoscopic shearography with radial sensitivity [26], or inspection of soft tissue phantoms [27].

The aforementioned results in shearography, especially with a single optical path are quite encouraging, but the flexibility of those solutions for the surface strain measurement of highly curved surfaces can be improved. The development of modern digital light projectors provides the ability to use these relatively small devices for in-line object shape measuring without significant system complication. This is a step back from the joint optical design or single optical path approach, but the benefits that are demonstrated in this paper are promising.

In this paper, a general solution to the strain inspection of free-form objects is presented. This includes in-line shape measuring, an estimation of the actual shear distances in 3D, sensitivity matrix correction, and a direct calculation of the surface strain components for each point of the point cloud, which represents the object. For the experimental part, a 3D shape shearography prototype was developed, equipped with three spatially distributed shearing cameras, one illumination laser source, and a structured light projector for in-line shape measuring. Preliminary findings were reported earlier [28,29].

Similar inspections of curved shapes with ESPI were previously reported where a photogrammetric image analysis from several cameras or digital image correlation (DIC) were used for the shape reconstruction [30–32]. In general, ESPI and shearography are similar speckle interferometry techniques; however, the additional variation of the shear distances for shearography makes the inspection of curved shapes more challenging than with ESPI.

A comment has to be made about the term "3D," which is used in the literature for 3D shearography [4,33,34] and 3D ESPI [35–37]. The "3D" term in these papers is used to emphasize the 3D nature of the surface strain vectors and not the 3D shape of the object. Most of the reported 3D systems were used to characterize (nearly) flat objects. So a new term "3D shape shearography" is proposed in the current paper to define shearography systems capable of measuring and precise mapping of the surface strain components onto curved objects.

2. SHEAROGRAPHY THEORY

During measurements with shearography a speckle pattern is generated by illuminating a rough surface with an expanded laser beam. Speckle interferograms are recorded by a camera with a shearing device [Fig. 1(a)] in two or more surface states, e.g., before and after deformation. The object can be deformed by thermal or mechanical loading. The shearing device duplicates the camera field of view, generating a sheared image, where two surface points P and Q [Fig. 1(b)], are combined at one point on the camera sensor. For a non-planar surface, surface points $P(x,y,z)$ and $Q(x+dx,y+dy,z+dz)$ are separated by the shear distance d_1, which has three orthogonal components (dx,dy,dz) in the object coordinate system (x_o,y_o,z_o), where subscript 1 refers to camera 1. For the initial surface state, reference interferograms are recorded and a phase-shift algorithm can be used to obtain the initial phase difference at the camera pixel ϕ_1^{initial}.

In practice, if the surface strain growth is relatively slow, the shear in the x- and y-directions, d_{x1} and d_{y1}, respectively, can be applied one after another and interferograms corresponding to each direction are recorded. More complicated optical schemes can be used to obtain interferograms with a shear in both directions simultaneously [38].

When the surface is deformed, points P and Q move to their new positions, P' and Q' respectively, and signal interferograms are recorded to get the signal difference of phase ϕ_1'. The surface deformation changes the length of the optical path from the laser located at S to the object surface points P and Q then to the first camera located at C_1 [Fig. 1(b)] [2]. For a small

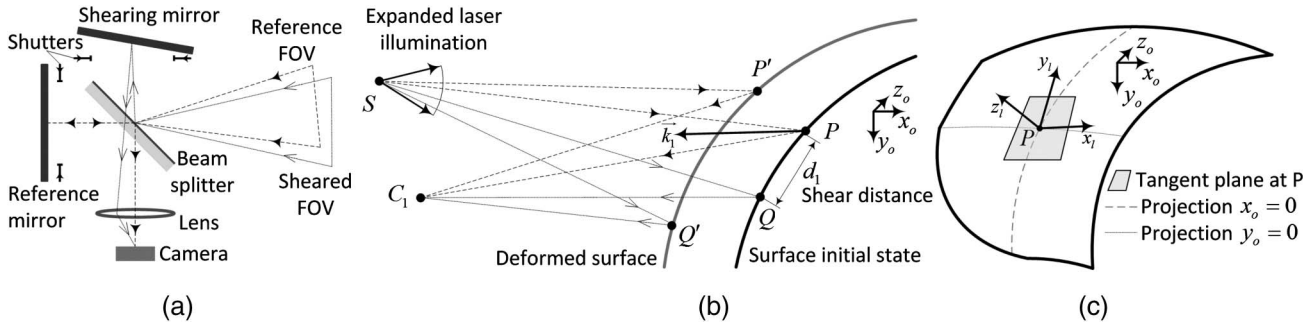

Fig. 1. Schematic representation of shearography principle in 3D: (a) optical paths in shearing device based on a Michelson interferometer and (b) optical paths differences when the surface is deformed; (c) the relation of local coordinate system (x_l,y_l,z_l) to the object coordinate system (x_o,y_o,z_o).

amount of shear in the y-direction d_{y1} (defined as $|d_{y1}| \ll |\overrightarrow{PC_1}|$ and $|d_{y1}| \ll |\overrightarrow{PS}|$) the change in optical path length causes the phase change $\Delta\phi_{y1}$ where the subscript 1 refers to the camera 1. The phase change $\Delta\phi_{y1}$ can also be calculated as a function of the surface strain components $(\partial u/\partial y, \partial v/\partial y, \partial w/\partial y)$ [2]:

$$\Delta\phi_{y1} = \phi'_{y1} - \phi_{y1}^{\text{initial}} = \frac{2\pi}{\lambda}\left(k_{x1}\frac{\partial u}{\partial y} + k_{y1}\frac{\partial v}{\partial y} + k_{z1}\frac{\partial w}{\partial y}\right)d_{y1}, \tag{1}$$

where $\phi_{y1}^{\text{initial}}$ and ϕ'_{y1} are the reference and signal phase differences obtained at the camera 1 at the initial surface state and after the load, respectively, λ is the laser wavelength, (k_{x1}, k_{y1}, k_{z1}) are components of the sensitivity vector k_1 of the camera 1, that is the bisector between the illumination PS and viewing PC_1 directions [Fig. 1(b)]:

$$\vec{k}_1 = \frac{\overrightarrow{PS}}{|\overrightarrow{PS}|} + \frac{\overrightarrow{PC_1}}{|\overrightarrow{PC_1}|}. \tag{2}$$

In order to isolate the surface strain components, a multi-component shearography instrument with at least three viewing directions (three cameras) needs to be used [4,5]. The surface strain components $(\partial u/\partial y, \partial v/\partial y, \partial w/\partial y)$ for the shear d_{yj} in the y-direction can be calculated [2,39] by processing the phase changes $\Delta\phi_{yj}$ obtained at each camera $j = 1, 2, 3$:

$$\begin{bmatrix} \frac{\partial u}{\partial y} \\ \frac{\partial v}{\partial y} \\ \frac{\partial w}{\partial y} \end{bmatrix} = \frac{\lambda}{2\pi} M^{-1} \begin{bmatrix} = \frac{\Delta\phi_{y1}}{d_{y1}} \\ \frac{\Delta\phi_{y2}}{d_{y2}} \\ \frac{\Delta\phi_{y3}}{d_{y3}} \end{bmatrix}$$

$$= \frac{\lambda}{2\pi} \begin{bmatrix} k_{x1} & k_{y1} & k_{z1} \\ k_{x2} & k_{y2} & k_{z2} \\ k_{x3} & k_{y3} & k_{z3} \end{bmatrix}^{-1} \begin{bmatrix} \frac{\Delta\phi_{y1}}{d_{y1}} \\ \frac{\Delta\phi_{y2}}{d_{y2}} \\ \frac{\Delta\phi_{y3}}{d_{y3}} \end{bmatrix}, \tag{3}$$

where M is a sensitivity matrix of sensitivity vector components for each camera. The surface strain components in the x-direction $(\partial u/\partial x, \partial v/\partial x, \partial w/\partial x)$ can be calculated in the same way replacing y by x in Eqs. (1) and (3) [4].

In case of a flat object, its coordinate system (x_o, y_o, z_o) coincides with the surface local coordinate system (x_l, y_l, z_l) [Fig. 1(c)] and two normal strains ε_{xx}, ε_{yy} in the x_l-, y_l-directions which are commonly used in practice are defined as

$$\varepsilon_{xx} = \frac{\partial u}{\partial x}, \qquad \varepsilon_{yy} = \frac{\partial v}{\partial y}. \tag{4}$$

When the object is curved as in Fig. 1(c), Eq. (4) has to be added with a coordinate transformation from the object coordinate system (x_o, y_o, z_o) to the local one (x_l, y_l, z_l), which can be done by identifying tangent planes at each point [40].

3. 3D SHAPE SHEAROGRAPHY

The proposed approach for the surface strain measuring of curved objects by 3D shape shearography (Fig. 2) is based on transferring shearography data from the shearography system with three shearing cameras to each point of the point cloud in three main steps:

1. In-line object shape measurement using geometric fringe projection (steps 1.1–1.3 in Fig. 2, Section 3.A) to get a point cloud representing the object shape. This is a key step that matches the shape of the object together with the shearography system geometry. This matching is used to correct the sensitivity matrix (step 1.4), to estimate shear in 3D and to map the strain maps.
2. Estimation of the actual shear distances in 3D for each shearing camera (steps 2.1–2.2 in Fig. 2, Section 3.B) mapped onto the curved surface, which is required for accurate numerical interpretation of phase maps.
3. The object loading and conventional shearography with registration of the phase changes $\Delta\phi_{xj}$ and $\Delta\phi_{yj}$ (step 3 in Fig. 2, Section 3.C) with temporal or spatial phase shifting, phase filtering and unwrapping, zero-order fringe tracking.

All these steps have to be done for each point P that is of interest for strain calculation in order to obtain parameters needed for Eq. (3).

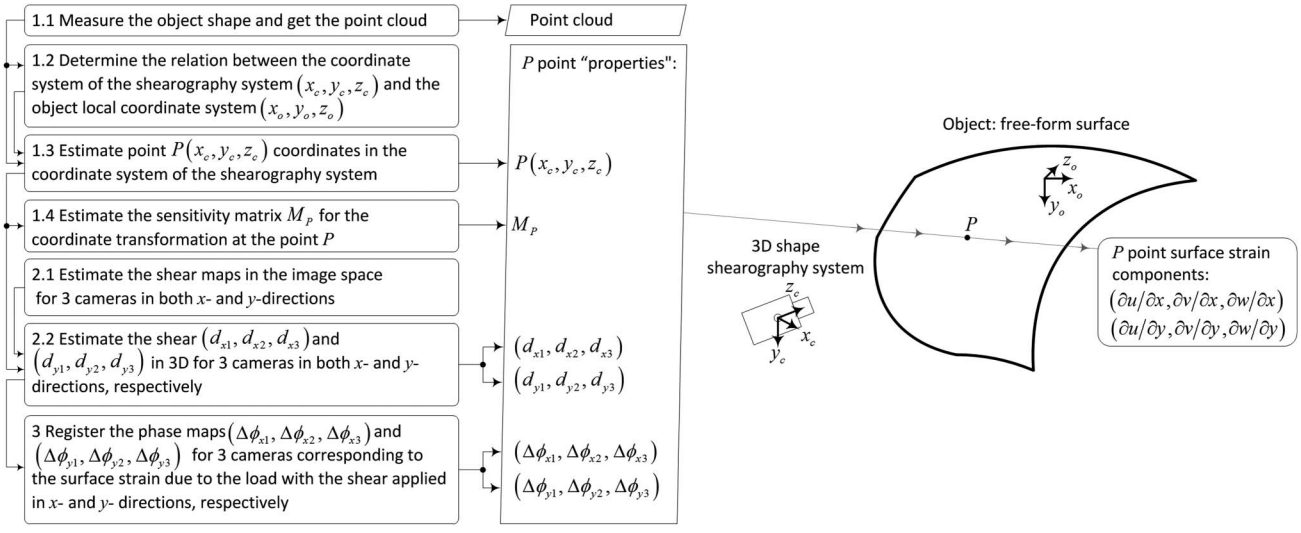

Fig. 2. Approach for surface strain measurement of free-form surfaces with 3D shape shearography.

A. Step 1. Cameras and Projector Geometric Calibration and Object Shape Measuring with Fringe Projection

In order to measure the shape of the surface (step 1), the cameras and the projector require a geometric calibration. The well-known Zhang's camera model [41] was used for this purpose together with commonly used toolboxes [42,43]. The projector was calibrated using the same model, but acting as an inverse camera.

The global calibration of three cameras and the projector (as an inverse camera) was done using the multiple view computer vision approach [44]. First, the cameras intrinsic parameters were identified in a conventional way [42]. Then, a global optimization procedure was performed to redefine both the extrinsic and the intrinsic parameters of the cameras and the projector by minimizing the reprojection error [29,44]. The reprojection error is the size of an uncertainty area when a reconstructed point P is projected to the cameras and compared with its position in the original images. During the calibration, a predefined checkerboard was projected onto a flat surface and captured by the cameras at different surface orientations. The corners of the checkerboard were used for the reprojection with a condition of belonging to one plane in 3D.

The 3D shape shearography system geometry can be calibrated based on the reference optical paths of shearing cameras. The reference paths were set by blocking the shutters in the shearing arm of each interferometer [Fig. 1(a)]. The calibration of reference paths is acceptable in practice because the shearography principle introduces coordinate uncertainty within the shear distance. Also, the orientation of the shear mirror is less stable over time than the fixed reference one especially when a piezo actuator is used.

Once the cameras and projector geometric calibration is done (as shown in Fig. 3), four matrices of intrinsic A_j and extrinsic $[R_j|T_j]$ parameters for each camera and the projector are known [41,42]. They are used for coordinate transformation from the homogeneous coordinates $[x \quad y \quad z \quad 1]^T$ of the point P in the object coordinate system (x_o, y_o, z_o) to the homogeneous coordinates of a point p_j in the cameras image coordinate system $[\alpha \quad \beta \quad 1]^T$ [Fig. 4(a)]:

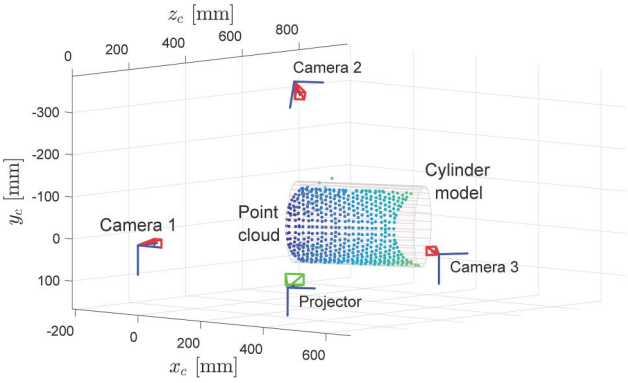

Fig. 3. Results of the cameras-projector geometry calibration with the point cloud measured with the fringe projection and a fitted cylinder model.

$$s_j p_j = A_j \begin{bmatrix} R_j & T_j \end{bmatrix} P, \tag{5}$$

where R_j and T_j are the rotation matrix and translation vector, respectively, s_j is a scale factor, and $j = 1, 2, 3, 4$ are the cameras and the projector internal numbers.

One of the cameras, e.g., the camera 1 coordinate system (x_{c1}, y_{c1}, z_{c1}) can be used as the master coordinate system (x_c, y_c, z_c) of the shearography instrument. In this case, the relationship between the coordinate systems of the remaining cameras ($j = 2, 3, 4$), the projector, and the camera 1 for a point P_{cj} is defined as [44]

$$P_c = P_{c1} = \begin{bmatrix} R_j^{-1} & -R_j^{-1} T_j \\ 0 & 1 \end{bmatrix} P_{cj}. \tag{6}$$

The object global (x_o, y_o, z_o) and local (x_l, y_l, z_l) coordinate systems have to be defined to relate the measured surface strain components to the object localized data (e.g., from strain gauges or numerical modeling) [Fig. 1(c)]. In the case of a flat object, these coordinate systems coincide; however, for a curved object a reconstruction of tangent planes is needed [40]. A mechanical reference or some surface point together with an axis of symmetry, if applicable, can be used to define (x_o, y_o, z_o) by a rotation matrix R_o and a translation vector T_o:

$$P_o = \begin{bmatrix} R_o & T_o \\ 0 & 1 \end{bmatrix} P_c. \tag{7}$$

The object shape can be measured with the common fringe projection technique by projecting predefined phase-shifted fringes (e.g., sinusoidal) onto the object [45] and presented as a point cloud of data points in 3D space (Fig. 3). The 3D shape shearography system has a benefit of using all three or more cameras during the fringe projection resulting in a potentially high accuracy of the shape measurement in comparison with conventional stereo-systems.

Once the point cloud is generated and the relationships between the coordinate systems are known, the sensitivity matrix M [Eq. (3)] can be corrected by simple use of coordinates for each point P in (x_o, y_o, z_o) (Fig. 3) and the system geometry represented by the cameras extrinsic parameters $[R_j|T_j](j = 1, 2, 3)$ [2,39] using Eqs. (2) and (3). Following the proposed approach (Fig. 2), a sensitivity matrix value M_P has to be assigned as a property to each point P of the cloud.

B. Step 2. Shear Estimation in 3D

As reported earlier [2,24], the shear angle of a shearing device may be not uniform across the field of view because of aberrations and wavefront errors of the interferometer mirrors and the beam splitter [Fig. 1(a)], and therefore the actual shear distances require calibration. This task becomes more complicated when the shear is mapped onto a curved object because of the varying dz component and differences in scale along z_{cj} [Fig. 1(b)]. It is proposed here to estimate the shear distance for each data point of the cloud in 3D by projecting it to each camera, identifying the shear in the image space of each camera (in pixels), and reprojecting it back onto the surface, as depicted in Fig. 4. The detailed explanation is given below.

Prior to the shear estimation in 3D it has to be identified in 2D, e.g., with DIC in the image space (α_j, β_j) of each

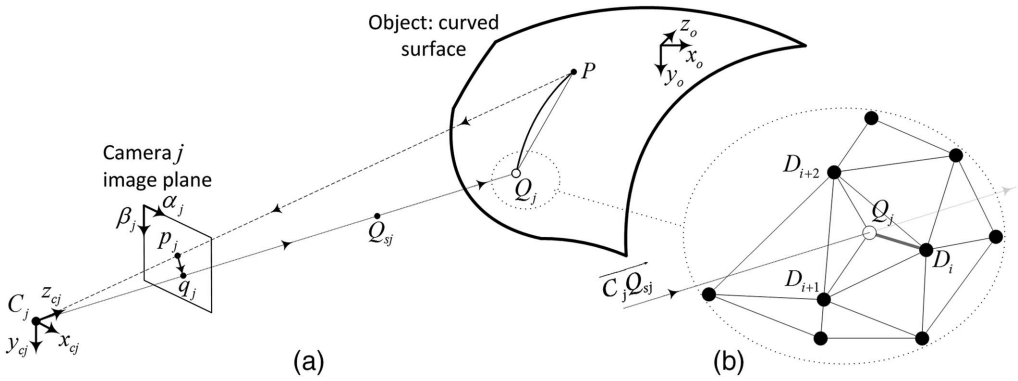

Fig. 4. Estimation of a shear map for 3D point cloud: (a) shear projection and (b) intersection of the reprojected "sheared" ray with the object surface.

camera [2,40]. For that, a predefined digital speckle pattern can be projected onto the object by the projector. Three images for each camera have to be taken through the reference paths (when the shear mirrors are blocked), and through the shear paths with shear applied sequentially in the x- and y-directions (when the reference mirrors are blocked). Digital image correlation of the reference images with the speckle pattern captured with shear in the x- and y-directions gives an estimation of the shear distances for each pixel of each camera, namely a 2D shear map [e.g., a sheared pixel q_j for the reference pixel p_j in Fig. 4(a)].

The shear distance in 3D can be found by reprojecting the sheared point q_j back to the point cloud; however, the exact scale value s_j is unknown for that [Eq. (5)]. The reprojection can be done with an arbitrary non-zero scale to define a ray $\overrightarrow{C_jQ_{sj}}$ and then to find its intersection with the point cloud. Assuming that p_jq_j is the shear amount in the image space for pixel p_j estimated with the digital image correlation, a point Q_{sj} can be identified in (x_o, y_o, z_o) by inverting Eq. (5) and performing an additional coordinate transformation from the camera j coordinate system to the object coordinate system (x_o, y_o, z_o):

$$Q_{s1} = \begin{bmatrix} R_o & T_o \\ 0 & 1 \end{bmatrix} \begin{bmatrix} R_j^{-1} & -R_j^{-1}T_j \\ 0 & 1 \end{bmatrix} \begin{bmatrix} A_j^{-1}s_jq_j \\ 1 \end{bmatrix}. \quad (8)$$

The intersection of the ray $\overrightarrow{C_jQ_{sj}}$ with the object surface has to be discovered. At least three algorithms can be used for that, including a simple search of the nearest point of the point cloud, a parametric search (if the surface can be parametrically defined), and a triangulation of the ray intersection within each facet of the point cloud [Fig. 4(b)].

Once the intersection point Q_j is found for each point of the cloud for the shear maps in the x- and y-directions, the shear distances $\overline{PQ_j}$ for each point P and camera $j = 1, 2, 3$ can be directly calculated and stored as a set of parameters (d_{x1}, d_{x2}, d_{x3}) and (d_{y1}, d_{y2}, d_{y3}). The shear distances in 3D are required for the calculation of the surface strain components [Fig. 2, Eq. (3)].

C. Step 3. Object Loading and Conventional Shearography with Estimation of the Surface Strain Components

The last step is to load the object thermally or mechanically and to register the phase changes $\Delta\phi_j$ corresponding to the surface deformation for the shear in the x- and y-directions for each camera $j = 1, 2, 3$, as described in Section 2. This may be done in a conventional way, that has been reported in detail for 3D shearography systems with multiple viewing configurations [2–4,23].

The estimation of the surface strain components requires absolute values of the phase maps $\Delta\phi_j$ [Eq. (1)] from all cameras. However, depending on the loading amount the phase change $\Delta\phi_j$ may exceed the range of $[0, 2\pi]$ or $[-\pi, \pi]$, which results in phase jumps of 2π. If so, an additional processing step, phase unwrapping, removes these phase jumps [2]; however, in most cases the absolute value of the phase is lost. Multiple additions of 2π, where needed, remove the phase jumps, but the absolute value gets lost. A possible solution is to track the zero-order fringe (zone of phase distribution corresponding to a zero surface displacement) as it was reported in the literature [2,46].

Following the proposed approach for the surface strain measuring of curved surfaces (Fig. 2), the registered and unwrapped absolute phase maps $(\Delta\phi_{x1}, \Delta\phi_{x2}, \Delta\phi_{x3})$ and $(\Delta\phi_{y1}, \Delta\phi_{y2}, \Delta\phi_{y3})$ for the shear applied in the x- and y-directions have to be assigned to the points in 3D. For that, a point of interest P is projected to each camera $j = 1, 2, 3$ using Eq. (5) to identify its pixel coordinates $p_j(\alpha_j, \beta_j)$ on the cameras sensors, then the corresponding values of the registered phase maps $\Delta\phi_{xj}(\alpha_j, \beta_j)$ and $\Delta\phi_{yj}(\alpha_j, \beta_j)$ are assigned to the projected point P as additional properties.

By this moment and according to the proposed approach (Fig. 2), any point P gets the complete set of properties that is required for the surface strain components calculation $(\partial u/\partial x, \partial v/\partial x, \partial w/\partial x)$ and $(\partial u/\partial y, \partial v/\partial y, \partial w/\partial y)$ using Eq. (3). The set includes

- the point coordinates (x_c, y_c, z_c);
- calculated sensitivity matrix M_P reflecting the instrument geometry;
- the shear values in 3D (d_{x1}, d_{x2}, d_{x3}) and (d_{y1}, d_{y2}, d_{y3}); and

• the phase values $(\Delta\phi_{x1}, \Delta\phi_{x2}, \Delta\phi_{x3})$ and $(\Delta\phi_{y1}, \Delta\phi_{y2}, \Delta\phi_{y3})$.

4. EXPERIMENTAL EVALUATION

A. 3D Shape Shearography System Prototype

For the experimental evaluation of the proposed approach for the surface strain measuring of curved surfaces, a 3D shape shearography system prototype was developed (Fig. 5) [47,48]. Three spatially distributed shearing cameras, a laser with beam expansion optics, and the projector were placed in a "T" configuration using an Alufix modular fixture system. A Torus laser from LASER QUANTUM with an optical power of 500 mW and a wavelength of 532 nm was used. Shearing cameras consisted of Basler Pilot piA2400 cameras with Linos MeVis-C 1.6/25 imaging lenses (apertures set to 1/8) and the shearing devices were based on Michelson interferometers [Fig. 1(a)]. An integrated structured light projector (LightCrafter DLP45000 from Texas Instruments) was used for the in-line shape measuring with fringe projection. For shearography, shearing and temporal phase shifting were performed by controlling the shearing mirrors in each camera with three coordinate piezo-electric actuators PSH 4z from Piezosystem Jena. The five-step phase-shifting method was found to be a rational compromise between the number of phase steps and the resulting accuracy.

The cameras and the projector were globally calibrated as a multiple-view computer vision system [42,43] in a volume of 200 × 150 × 150 mm (Section 3, Fig. 3). As a result of the global calibration, a reprojection error for the three cameras was less than 2.7 pixels (RMSE) corresponding to the triangulation error of 0.2 mm. The triangulation error defines the overall spatial resolution of the 3D shape shearography instrument when interferometric phase values from three cameras are combined at each point of the point cloud.

A previously reported, a cylinder specimen with a length of 400 mm and an external diameter of 190 mm was used as a test object [23,24]. The specimen was mounted in front of the system at a distance of 500 mm and was loaded by internal pressure with a pump using oil. Several strain gauges were mounted on the specimen to provide reference values for the normal strains ε_{xx} and ε_{yy} in the x_l-, y_l-directions, respectively.

B. Experimental Results

The shape of the specimen was measured as proposed in Subsection 3.A using the fringe projection with a five-step Schwider–Hariharan phase-shifting algorithm [49]. First, pre-generated sinusoidal fringes were projected on the specimen and captured through the reference optical paths [Fig. 1(a)]. Second, the geometric phase maps from the cameras were unwrapped with the branch-cut method [50] and co-registered using an additional projected image with a bright spot at the center of the projector field of view. Then, the pixel coordinates from three cameras and the projector with the same geometric phase values were used for a direct multiple-view triangulation of the point cloud [44]. Once the point cloud was calculated, the cylinder coordinate system (x_o, y_o, z_o) was aligned with the axis of symmetry of a fitted parametric cylinder model [Fig. 5(a)].

The actual shear distances were estimated for each point of the cloud as proposed in Subsection 3.B. The shear maps in the image space of the cameras were estimated by projecting a predefined speckle pattern by the projector and processing of images taken through the reference and sheared optical paths with the 2D image correlation technique [Fig. 6(a)].

Shear distances in 3D were estimated with three different algorithms. The first, the simplest, is a search of the nearest point [e.g., D_i in Fig. 4(b)]. For that, the point cloud density should be high enough (in our practice less than 0.05 mm). However, this simple approach results in areas with step variations of the shear distances in 3D [low contrast radial fringes in Fig. 6(b)]. This happens when a smooth continuous 2D shear map [Fig. 6(a)] is reprojected on a regularized point cloud. These step variations are also shown in zoom into the cross sections with the shear distances in Fig. 6(e) with

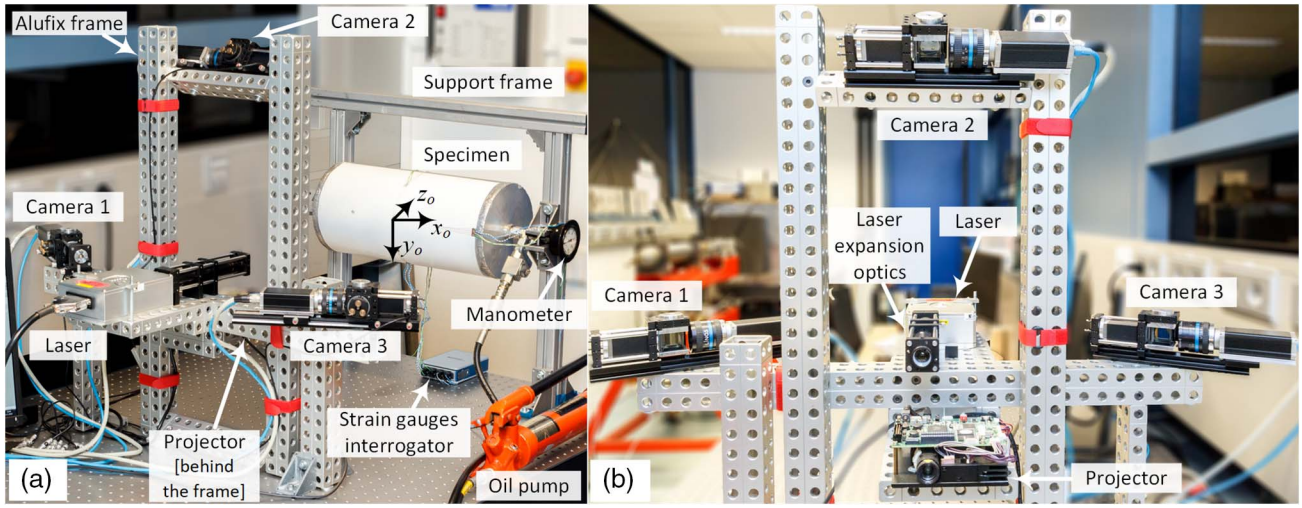

Fig. 5. 3D shape shearography system prototype (a) with the cylinder specimen in front of it and (b) as seen from the specimen. The cameras-projector geometry is also shown in Fig. 3.

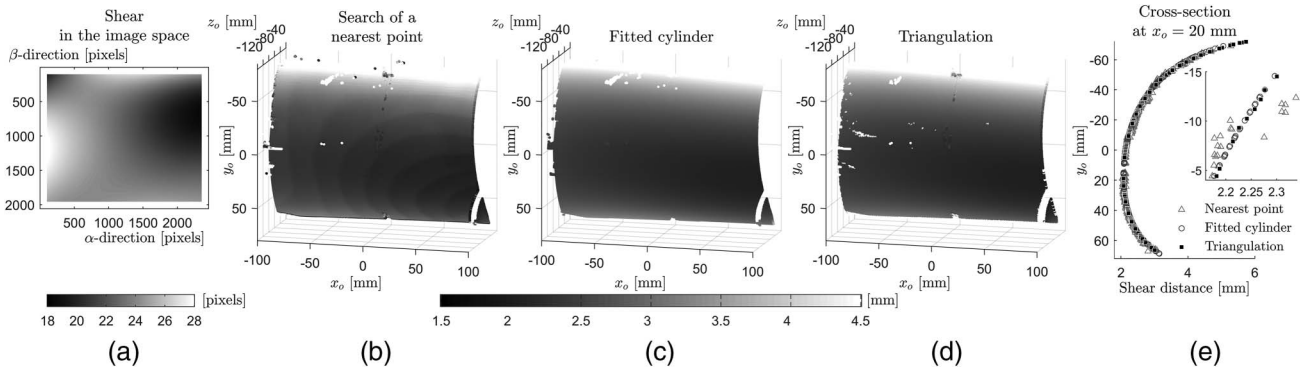

Fig. 6. Shear distances estimated for camera 1 in the y-direction: (a) 2D shear map in the camera image space identified with DIC, shear in 3D (b) by searching the nearest point of the point cloud, (c) by intersection with a fitted cylinder model, and (d) by triangulation of the intersection within each facet with a cross section (e) revealing strain values at $x_o = 20$.

approximately 0.05–0.1 mm differences of the shear values estimated by the search of the nearest point at the bottom-left and top-right in comparison with two other algorithms.

The second algorithm is applicable if the object has a simple shape and a parametric surface can be fitted to the point cloud, and therefore the intersection of the ray $\overrightarrow{C_j Q_{sj}}$ with the surface can also be found parametrically [29,51,52]. In the case of a cylinder [Fig. 3(b)], a cylinder model was fitted into the data points using the RANSAC algorithm [53]. Results of the parametric shear calculation are presented in Figs. 6(c) and 6(e).

The third algorithm, which is more universal, is to identify a triangle that contains the intersection with the reprojected ray $\overrightarrow{C_j Q_{sj}}$ [e.g., $D_i D_{i+1} D_{i+2}$ in Fig. 4(b)] and to triangulate the intersection point within this triangle [54]. Triangulated shear distances are shown in Figs. 6(d) and 6(e).

A comparison of the three algorithms for the shear estimation in 3D is presented in Figs. 6(e) and 7 with an assumption that the parametric search provides the most reliable results for the cylindrical object, and therefore it was used as a reference. The third algorithm based on triangulation [Fig. 7(b)] has a significantly better performance than the search of the nearest point [Fig. 7(a)]. Also, the point cloud density can be lowered up to 1 mm without loss in accuracy of the shear reconstruction, which is beneficial for the processing time.

As proposed in Subsection 3.C during the strain measurements, the specimen was loaded by an internal pressure of 1.0 ± 0.1 MPa in a sequential mode [23] with steps of approximately 0.1 MPa controlled by a manometer. Such small load steps correspond to a phase change of less than 2π for reliable tracking of the zero-order fringe. At each load step five phase-shifted interferograms for the shear x- and y-directions were recorded [49]. After that, the total phase maps were calculated as a sum of all the steps and six surface strain components were calculated for each point of the entire point cloud according to Subsection 3.C [Figs. 8(a)–8(f)]. Each subplot is a 3D point cloud with a gray level corresponding to the strain level. The measured area is close to 200 × 130 mm in the $y_o x_o$-plane. The measured surface strain components $(\partial u/\partial x)$ and $(\partial v/\partial y)$ that are commonly used are enlarged in Figs. 8(e) and 8(f). A cross section in Fig. 8(g) shows the mapping of the surface

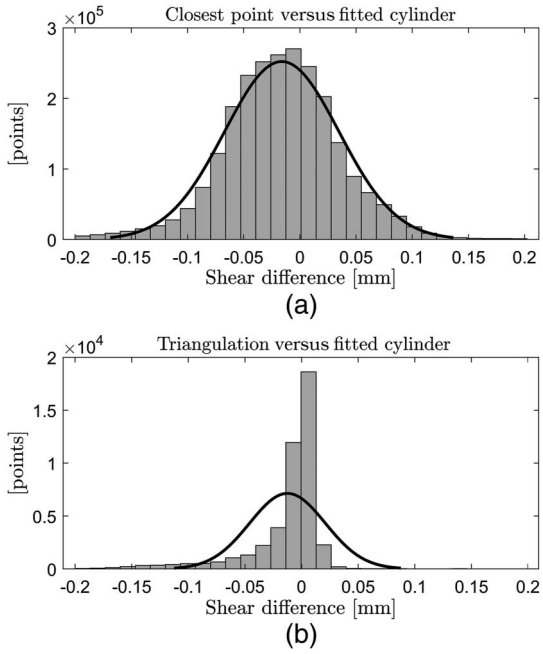

Fig. 7. Comparison of the shear distances in 3D for camera 1 in the y-direction estimated with the fitted cylinder and (a) the search the nearest point of the point cloud and (b) by triangulation of the intersection within each facet.

strain components over the cylinder. Zones with missing data at the center and top of the cloud correspond to locations where the strain gauges were mounted. Minor incomplete areas correspond to a high specular reflection.

The comparison of the surface strain components measured with the 3D shape shearography and four strain gauges is provided in Table 1. For that, the surface strain components $(\partial u/\partial x, \partial v/\partial x, \partial w/\partial x)$ and $(\partial u/\partial y, \partial v/\partial y, \partial w/\partial y)$ measured in (x_o, y_o, z_o) [Figs. 8(a)–8(f)] were mapped in (x_l, y_l, z_l) by identification of local tangent planes in each point of the point cloud [Fig. 1(c)]. Values from four strain gauges were averaged in time.

The overall effect of the proposed approach for 3D shape shearography is presented in Fig. 9. For that, $(\partial v/\partial y)$ was

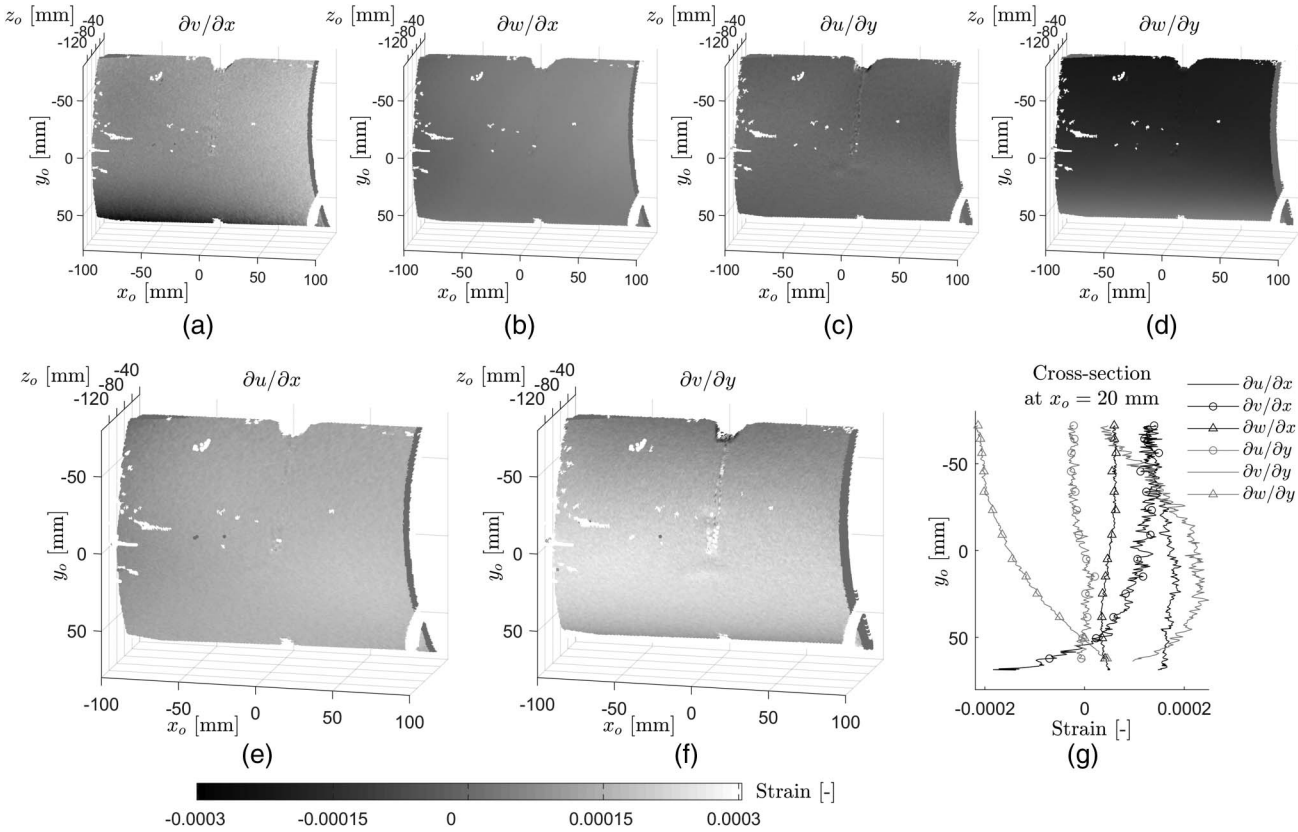

Fig. 8. Surface strain components in (x_o, y_o, z_o) mapped onto the point cloud (a)–(f) with a cross section (g) revealing strain values at $x_o = 20$.

Table 1. Comparison of Experimental Results Obtained with 3D Shape Shearography and Strain Gauges ($*10^{-6}$)

	3D Shape Shearography		Strain Gauges		
Normal Strain	Mean value	STD	Mean value	STD	Mean Difference
ϵ_{xx}	144	28	62	4	82
ϵ_{yy}	196	31	170	3	26

estimated (x_o, y_o, z_o) without any correction for the shape (fixed shear of 2.2 mm for the cameras 1 and 3, 1.8 mm for the camera 2, and constant sensitivity matrix corresponding to the center of the object at $x_o = y_o = z_o = 0$). Both not corrected and corrected $(\partial v/\partial y)$ in (x_o, y_o, z_o) were compared with the calculated normal strain ϵ_{yy} in (x_l, y_l, z_l) in Fig. 9(c). The comparison shows that in the center of the specimen, where the cylinder surface is close to a flat surface ($|y_o| < 20$ mm), the results before and after corrections are close. With the height increase, the not corrected strain significantly increases, as the increase in shearography phase for the cylinder specimen [23] is not compensated by the fixed shear. The recalculation of corrected $(\partial v/\partial y)$ in (x_o, y_o, z_o) to ϵ_{yy} in (x_l, y_l, z_l) reveals the improved uniformity of the mapped strain components close to the strain gauges values. The strains in the y-direction are presented as they are more affected by the cylinder curvature, than in the x-direction.

5. DISCUSSION

A new approach for the measurement of the surface strain components of curved objects by 3D shape shearography has been proposed. This approach is based on individual points of the point cloud acting as a "carrier" of the shearography data (see point properties in Fig. 2). A triangulated mesh can also be used, with a vertex face acting as the carrier keeping the same processing steps. The presented approach can also be applied to flat surfaces, especially when the surface is not normal to the system and the shear distance changes due to a difference in scale along the distance. If the shape of the object is known or its CAD model is available, the in-line shape measuring with fringe projection can be used for estimation of the object orientation. A realization of the approach based on a multiple viewing shearography system with three shearing cameras and one illumination source has been presented. It can, however, be adapted to a higher number of cameras or a multiple illumination concept.

The accuracy of the cameras-projector calibration directly defines the performance of the 3D shape shearography instrument. Based on our experience with the 3D shape shearography setup (Fig. 5) the triangulation error should be less than 1 mm. This practical requirement determined the need of the global calibration procedure using the multiple-view computer vision approach. Initially, the cameras and the projector were calibrated in pairs as stereovision systems (cameras 1 + 2, 1 + 3, 1 + projector) [28,55]. As a result of multiple coordinate systems conversions, the

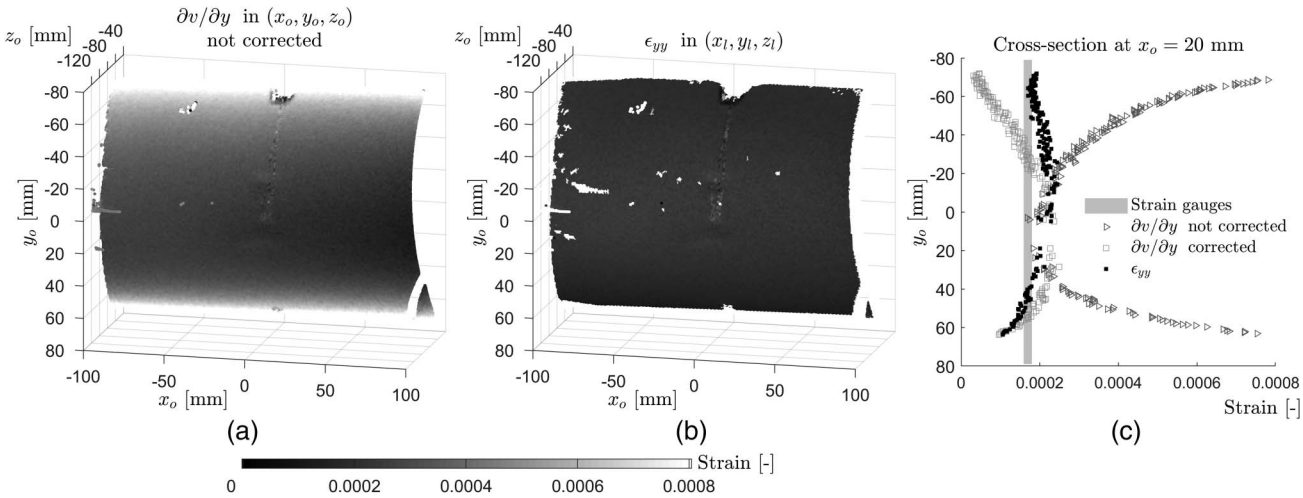

Fig. 9. (a),(b) Comparison of $(\partial v/\partial y)$ mapped in (x_o, y_o, z_o) calculated without any correction for the shape (fixed shear and the sensitivity matrix) and the final estimation of ϵ_{yy} in (x_l, y_l, z_l) with a cross section (c) revealing strain values at $x_o = 20$, also for corrected $(\partial v/\partial y)$ in (x_o, y_o, z_o) taken from Figs. 8(f) and 8(g). Extended color range in comparison with Fig. 8.

triangulation error reached 3 mm in the worst cases. This error introduced uncertainty to the transfer of all parameters to the point cloud (Fig. 2).

An assumption was made when the actual shear distance was estimated in 3D [Fig. 4(a)] as the chord $\overline{PQ_j}$ was determined, not the arc PQ_j. This is applicable in practice, as the additional error of shear estimation is less than 5% when the shear distance is 5 mm and local radius of curvature is 5 mm. In the case of higher radiuses and smaller shear distances, the error of local surface flattening is almost negligible.

The residual non-flatness of the normal strain ϵ_{yy} in Figs. 9(b) and 9(c) is a probable result of uncertainties of the shear estimation in 2D [Fig. 6(a)]. An improvement of the uniformity in 2D can be achieved by use of more precise optical elements (mirrors, beam splitter) in the shearing interferometers. A relatively high mean difference (Table 1) between the results obtained with the 3D shearography prototype and strain gauges may be explained by a low absolute level of the measured strain and insufficient system calibration. Further experiments at higher strain levels with various curved objects (e.g., leading edges) are planned to explore the new technique.

The cylinder specimen was used for the experiments as a compromise in the specimen complexity. The cylindrical specimen has a radial symmetry which is practical to analyze the uniformity of the shear maps in 3D (Fig. 6) and the symmetry and uniformity of the surface strain components about the x_o-axis (as in Figs. 8 and 9). However, the presented approach of 3D shape shearography can be applied to various curved or free-form smooth surfaces, which can be reliably measured with the fringe projection and provide smooth shearography phase maps.

The proposed combination of the fringe projection with the shearography resulting in 3D shape shearography also fuses the drawbacks of both techniques. One of them is the dependence of fringe projection and computer vision systems in general on the distance from the system. Normally the accuracy of the shape measurement decreases with the distance, which is expected to affect the overall performance in 3D shape shearography. In practice, the apertures of imaging lenses in shearography are set to 1/4…1/10 to increase the speckle size in the image space for a reliable shearography phase reconstruction. This also helps for reliable shape measurements of curved and free-form objects as the depth of view is increased. The overall fusion of drawbacks will be explored in the future during optimization of the new technique.

6. CONCLUSIONS

This paper presents a new approach of 3D shape shearography for strain inspection of curved objects. This approach is based on the integration of a structured light projector into the 3D shearography system for in-line shape measuring. As a result, the actual shear distances along the curved object can be estimated together with a correction of the sensitivity matrices for calculation of the surface strain components.

The proposed approach can improve the overall performance of the shearography technique. The new ability to perform an inspection of 3D and free-form surfaces may open new applications and lead to practical solutions of new tasks in crucial fields, such as aerospace (e.g., inspection of leading edges and nose cone of aircraft), energy (e.g., turbine blades), and cultural heritage (e.g., sculptures). At the same time a higher accuracy of measurement of the surface strain components, mapped onto curved surfaces, may lead to better characterization of materials and more reliable detection of inner defects.

Experimental results obtained with the cylinder specimen prove the applicability of the approach; however, some improvements have to be done. The next steps of the research are to improve the uniformity of the shear maps in 2D and to employ an additional viewing direction for robust absolute phase and consequently, absolute strain reconstruction [56,57].

Some of the algorithms used in this paper (e.g., the fringe-projection, cameras-projection calibration) can be improved by employing more advanced or recent technical solutions.

The main aim of this paper was to present the developed approach using the commonly used techniques. Optimization of each processing step is also a subject for the future work.

Funding. Horizon 2020 Framework Programme (H2020) (GA 636549).

Acknowledgment. The project "EXTREME" leading to this paper has received funding from the European Union's Horizon 2020 research and innovation program under agreement No. 636549.

REFERENCES

1. Y. Y. Hung, "Shearography: a new optical method for strain measurement and non-destructive testing," Opt. Eng. **21**, 213–391 (1982).
2. W. Steinchen and L. Yang, *Digital Shearography: Theory and Application of Digital Speckle Pattern Shearing Interferometry* (SPIE, 2003).
3. D. Francis, R. P. Tatam, and R. M. Groves, "Shearography technology and applications: a review," Meas. Sci. Technol. **21**, 102001 (2010).
4. S. W. James and R. P. Tatam, "Time-division-multiplexed 3D shearography," Proc. SPIE **3744**, 394–403 (1999).
5. R. M. Groves, S. W. James, and R. P. Tatam, "Multi-component shearography employing four measurement channels," Proc. SPIE **4933**, 135–140 (2003).
6. K. A. Stetson, "Use of sensitivity vector variations to determine absolute displacements in double exposure hologram interferometry," Appl. Opt. **29**, 502–504 (1990).
7. R. M. Groves, S. W. James, and R. P. Tatam, "Strain measurement in curved industrial components using multicomponent shearography," Proc. SPIE **4398**, 216–224 (2001).
8. H. M. Shang, C. Quan, C. J. Tay, and Y. Y. Hung, "Generation of carrier fringes in holography and shearography," Appl. Opt. **39**, 2638–2645 (2000).
9. H. M. Shang, Y. Y. Hung, W. D. Luo, and F. Chen, "Surface profiling using shearography," Opt. Eng. **39**, 23–31 (2000).
10. R. M. Groves, S. W. James, and R. P. Tatam, "Shape and slope measurement by source displacement in shearography," Opt. Lasers Eng. **41**, 621–634 (2004).
11. P. Blain, F. Michel, P. Piron, Y. Renotte, and S. Habraken, "Combining shearography and interferometric fringe projection in a single device for complete control of industrial applications," Opt. Eng. **52**, 084102 (2013).
12. E. K. Hack and M. Riner, "3D ESPI and 3D shearography measurements applied to NDT and FEM analysis validation for industrial quality control," Proc. SPIE **4398**, 155–167 (2001).
13. R. M. Groves, A. Li, X. Liu, S. Hackney, X. Peng, and W. Osten, "2.5 D virtual reality visualisation of shearography strain data from a canvas painting," Proc. SPIE **7391**, 739109 (2009).
14. A. G. Baldjiev and V. C. Sainov, "Fault detection by shearography and fringes projection techniques," in *Fringe 2013: 7th International Workshop on Advanced Optical Imaging and Metrology* (Springer, 2014), pp. 519–522.
15. D. Buchta, N. Hein, G. Pedrini, C. Krekel, and W. Osten, "Combination of topology and structural information for damages and deterioration analysis of artworks," Proc. SPIE **9527**, 95270Q (2015).
16. P. Klausmeyer, M. Cushman, I. Dobrev, M. Khaleghi, E. J. Harrington, X. Chen, and C. Furlong, "Quantifying and mapping induced strain in canvas paintings using laser shearography," in *The Noninvasive Analysis of Painted Surfaces: Scientific Impact and Conservation Practice* (Smithsonian Contributions to Museum Conservation, 2016), pp. 1–13.
17. R. Huber and R. Berger, "Shearography as an industrial application including 3D result mapping," in *9th European Conference on Non-Destructive Testing* (2006), pp. 25–29.
18. R. Berger, "Quality control with shearography and 3D-digitizing," in *10th European Conference on Non-Destructive Testing* (2010).
19. P. S. Heckbert, "Survey of texture mapping," IEEE Comput. Graph. Appl. **6**, 56–67 (1986).
20. X. Chen, "Computational and experimental approach for non-destructive testing by laser shearography," Ph.D. thesis (University of Zaragoza, 2014).
21. X. Chen, M. Khaleghi, I. Dobrev, W. Tie, and C. Furlong, "Structural health monitoring by laser shearography: Experimental and numerical investigations," in *Experimental and Applied Mechanics, Volume 6: Proceedings of the 2014 Annual Conference on Experimental and Applied Mechanics*, N. Sottos, R. Rowlands, and K. Dannemann, eds. (Springer, 2015), pp. 149–155.
22. X. Chen, M. Khaleghi, I. Dobrev, and C. Furlong, "Non-destructive testing (NDT) by laser shearography and fringe projection," in *Society of Engineering Science, SES/ASME-AMD Summer Meeting*, Characterization and Imaging of Structural and Material Imperfections (Brown University, 2013).
23. D. T. Goto and R. M. Groves, "A combined experiment with simulation approach to calibrated 3D strain measurement using shearography," Proc. SPIE **7387**, 73871J (2010).
24. D. T. Goto and R. M. Groves, "Error analysis of 3D shearography using finite-element modelling," Proc. SPIE **7718**, 771816 (2010).
25. H. Hajská, P. Koštial, O. Kodym, Z. Jančíková, J. David, R. Meca, and V. Rusnák, "On shearography testing of tires separations," in *Mechanical and Materials Engineering of Modern Structure and Component Design* (Springer, 2015), pp. 97–114.
26. F. J. Macedo, M. E. Benedet, A. V. Fantin, D. P. Willemann, F. A. A. da Silva, and A. Albertazzi, "Inspection of defects of composite materials in inner cylindrical surfaces using endoscopic shearography," Opt. Lasers Eng. **104**, 100–108 (2017).
27. N. U. Sujatha and V. M. Murukeshan, "Nondestructive inspection of tissue/tissue like phantom curved surfaces using digital speckle shearography," Opt. Eng. **43**, 3055–3060 (2004).
28. A. G. Anisimov and R. M. Groves, "3D shape shearography with integrated structured light projection for strain inspection of curved objects," Proc. SPIE **9525**, 952517 (2015).
29. A. G. Anisimov, M. G. Serikova, and R. M. Groves, "Development of the 3D shape shearography technique for strain inspection of curved objects," in *Imaging and Applied Optics* (Optical Society of America, 2016), paper DTh3C.4.
30. D. Dirksen, J. Gettkant, G. Bischoff, B. Kemper, Z. Böröcz, and G. von Bally, "Improved evaluation of electronic speckle pattern interferograms by photogrammetric image analysis," Opt. Lasers Eng. **44**, 443–454 (2006).
31. R. Schwede, H. Babovsky, A. Kiessling, and R. Kowarschik, "Measurement of three-dimensional deformation vectors with digital holography and stereophotogrammetry," Opt. Lett. **37**, 1943–1945 (2012).
32. M. Dekiff, P. Berssenbrügge, B. Kemper, C. Denz, and D. Dirksen, "Simultaneous acquisition of 3d shape and deformation by combination of interferometric and correlation-based laser speckle metrology," Biomed. Opt. Express **6**, 4825–4840 (2015).
33. S. W. James and R. P. Tatam, "3D shearography for surface strain analysis," Proc. SPIE **3783**, 247–256 (1999).
34. J. Molimard, W. Dandach, and P. Picart, "Direct strain and slope measurement using 3D DSPSI," in *PhotoMechanics* (Montpellier, 2013).
35. T. Fricke-Begemann and J. Burke, "Speckle interferometry: three-dimensional deformation field measurement with a single interferogram," Appl. Opt. **40**, 5011–5022 (2001).
36. T. Fricke-Begemann, "Three-dimensional deformation field measurement with digital speckle correlation," Appl. Opt. **42**, 6783–6796 (2003).
37. I. M. De. la Torre, M. D. S. H. Montes, J. M. Flores-Moreno, and F. M. Santoyo, "Laser speckle based digital optical methods in structural mechanics: a review," Opt. Lasers Eng. **87**, 32–58 (2016).
38. T. Siebert and B. Schmitz, "New shearing setup for simultaneous measurement of two shear directions," Proc. SPIE **3637**, 225–230 (1999).
39. D. Francis, S. W. James, and R. P. Tatam, "Surface strain measurement using multi-component shearography with coherent fibre-optic imaging bundles," Meas. Sci. Technol. **18**, 3583–3591 (2007).

40. M. A. Sutton, J. J. Orteu, and H. Schreier, *Image Correlation for Shape, Motion and Deformation Measurements* (Springer, 2009).
41. Z. Zhang, "Flexible camera calibration by viewing a plane from unknown orientations," in *7th IEEE International Conference on Computer Vision* (1999), Vol. **1**, pp. 666–673.
42. J. Heikkila and O. Silven, "A four-step camera calibration procedure with implicit image correction," in *IEEE Computer Society Conference on Computer Vision and Pattern Recognition* (1997), pp. 1106–1112.
43. J.-Y. Bouget, R. Silva, L. Pardini, and M. Rezende, "Camera calibration toolbox for MATLAB," http://www.vision.caltech.edu/bouguetj/calib_doc (2004).
44. R. Hartley and A. Zisserman, *Multiple View Geometry in Computer Vision* (Cambridge, 2003).
45. S. Zhang, "Recent progresses on real-time 3D shape measurement using digital fringe projection techniques," Opt. Lasers Eng. **48**, 149–158 (2010).
46. R. M. Groves, S. W. James, and R. P. Tatam, "Investigation of the fringe order in multi-component shearography surface strain measurement," in *Fringe 2005* (Springer, 2006), pp. 212–216.
47. B. Müller, A. G. Anisimov, J. Sinke, and R. M. Groves, "Thermal strains in heated fiber metal laminates," in *Emerging Technologies in Non-Destructive Testing VI (ETNDT)* (2015).
48. A. G. Anisimov, B. Müller, J. Sinke, and R. M. Groves, "Analysis of thermal strains and stresses in heated fibre metal laminates," Strain **54**, e12260 (2018).
49. P. Hariharan, B. F. Oreb, and T. Eiju, "Digital phase-shifting interferometry: a simple error-compensating phase calculation algorithm," Appl. Opt. **26**, 2504–2506 (1987).
50. D. C. Ghiglia and M. D. Pritt, *Two-Dimensional Phase Unwrapping: Theory, Algorithms, and Software* (Wiley, 1998), Vol. **4**.
51. D. L. Toth, "On ray tracing parametric surfaces," in *SIGGRAPH '85 12th Annual Conference on Computer Graphics and Interactive Techniques* (ACM, 1985), pp. 171–179.
52. D. Legland, "Graphics library geom3d," http://www.mathworks.com/matlabcentral/fileexchange/24484-geom3d (2009).
53. P. Torr and A. Zisserman, "MLESAC: a new robust estimator with application to estimating image geometry," Comput. Vision Image Understanding **78**, 138–156 (2000).
54. T. Möller and B. Trumbore, "Fast, minimum storage ray/triangle intersection," in *SIGGRAPH '05 ACM SIGGRAPH 2005 Courses* (ACM, 2005).
55. A. G. Anisimov, B. Müller, J. Sinke, and R. M. Groves, "Strain characterization of embedded aerospace smart materials using shearography," Proc. SPIE **9435**, 943524 (2015).
56. T. Siebert, K. Splitthof, and A. Ettemeyer, "A practical approach to the problem of the absolute phase in speckle interferometry," J. Holography Speckle **1**, 32–38 (2004).
57. T. O. H. Charrett, D. Francis, and R. P. Tatam, "Quantitative shearography: error reduction by using more than three measurement channels," Appl. Opt. **50**, 134–146 (2011).